UC San Diego

UC San Diego Previously Published Works

Title

INTERSTELLAR SCINTILLATION OF THE DOUBLE PULSAR J0737−3039

Permalink

https://escholarship.org/uc/item/4kr3g6pv

Journal

The Astrophysical Journal, 787(2)

ISSN

0004-637X

Authors

Rickett, BJ
Coles, WA
Nava, CF
et al.

Publication Date

2014-06-01

DOI

10.1088/0004-637x/787/2/161

Peer reviewed

eScholarship.org Powered by the California Digital Library
University of California

Draft version April 7, 2014
Preprint typeset using LaTeX style emulateapj v. 04/17/13

arXiv:1404.1120v1 [astro-ph.SR] 4 Apr 2014

INTERSTELLAR SCINTILLATION OF THE DOUBLE PULSAR J0737−3039

B. J. Rickett[1], W. A. Coles[1], C. F. Nava[1], M. A. McLaughlin[2,3], S. M. Ransom[4], F. Camilo[7,8], R. D. Ferdman[3,6], P. C. C. Freire[6,9], M. Kramer[3,9], A. G. Lyne[3], I. H. Stairs[5]

Draft version April 7, 2014

ABSTRACT

We report here a series of observations of the interstellar scintillation (ISS) of the double pulsar J0737−3039 over the course of 18 months. As in earlier work (Coles et al. 2005) the basic phenomenon is the variation in the ISS caused by the changing transverse velocities of each pulsar, the ionized interstellar medium (IISM), and the Earth. The transverse velocity of the binary system can be determined both by VLBI and timing observations. The orbital velocity and inclination is almost completely determined from timing observations, but the direction of the orbital angular momentum is not known. Since the Earth's velocity is known, and can be compared with the orbital velocity by its effect on the timescale of the ISS, we can determine the orientation Ω of the pulsar orbit with respect to equatorial coordinates ($\Omega = 65 \pm 2°$). We also resolve the ambiguity ($i = 88.7$ or $91.3°$) in the inclination of the orbit deduced from the measured Shapiro delay by our estimate $i = 88.1 \pm 0.5°$. This relies on analysis of the ISS over both frequency and time and provides a model for the location, anisotropy, turbulence level and transverse phase gradient of the IISM. We find that the IISM can be well-modeled during each observation, typically of a few orbital periods, but its turbulence level and mean velocity vary significantly over the 18 months.

Keywords: pulsars: general – pulsars: individual (J0737−3039) – ISM: general – binaries: general

1. INTRODUCTION

The double pulsar binary system J0737−3039 is in a highly relativistic orbit with significant eccentricity (Lyne et al. 2004). It is an eclipsing binary that is a wonderful laboratory for studies of general relativity (Kramer et al. 2006). Detailed measurements of the eclipses of A have been used to probe the magnetosphere of the B neutron star (McLaughlin et al. 2004; Lyutikov & Thompson 2005) and provide a measurement of geodetic precession (Breton et al. 2008). The changes in the pulse profiles have been used to explore the precession of the emission beams, the evolution of the orbital system and the dynamics of B's supernova (Stairs et al. 2006; Ferdman et al. 2013; Perera et al. 2010, 2012). It is also a fine system for study of the interstellar plasma (IISM) because the scattering is dominated by a compact region, the velocities are well determined, and the plasma turbulence can be probed on two neighbouring lines of sight.

Ransom et al. (2004) first reported how the interstellar intensity scintillation (ISS) of the A pulsar exhibits dramatic modulation in timescale over its orbital period (2.45 hr). Following the method proposed by Lyne (1984) and developed by Ord et al. (2002) for PSR J1141−6545, the authors estimated a rather high center of mass velocity for the double pulsar. Subsequent analysis of the same data showed that the scattering must be anisotropic and inclusion of this effect in the analysis greatly reduced the implied center of mass velocity (Coles et al. 2005) – hereafter Paper 1. In this paper we found correlation between the ISS of pulsars A and B near the time of A's eclipse by B. From the correlation we concluded that the orbital inclination angle was considerably closer to 90° than had been expected on the basis of the original measurements of the Shapiro delay (Lyne et al. 2004).

The main purpose of the observations reported here was to make use of the Earth's orbital velocity to improve, calibrate, and align the earlier scintillation analyses. This would allow us to correct the center of mass velocity for the motion of the Earth, to orient the binary orbit with respect to the celestial reference frame, and to locate the distance of the scattering region. The additional observations were also expected to improve the estimates of the inclination of the orbit, the anisotropy of the IISM and the spatial spectrum of the electron density of the IISM. However, two factors made the original plan of analysis impossible. First the phase at which emission from B is easily detectable drifted away from the time of A's eclipse during the course of the 2004-5 observations. This made measurements of the correlation between the A and B pulsars much less consistent and reliable than had been expected. Second we observed that, although the turbulence in the IISM is homogeneous over several binary orbits, it is not stationary over a year, nor is the velocity of the IISM constant over the year. This phenomenon was also observed by Ord [private communication] when his group attempted to observe the effect of the Earth's orbit on scintillations of PSR J1141−6545.

[1] ECE Dept., University of California San Diego, La Jolla, CA 92093-0407, USA; bjrickett@ucsd.edu
[2] West Virginia University, Morgantown, WV 26505, USA
[3] Jodrell Bank Center for Astrophysics, University of Manchester, M13 9PL, UK
[4] National Radio Astronomy Observatory, Charlottesville, VA 22903, USA
[5] Dept. of Physics and Astronomy, University of British Columbia, Vancouver, BC V6T 1Z1, Canada
[6] Dept. of Physics, McGill University, Montréal, QC H3A 2T8, Canada
[7] National Astronomy and Ionosphere Center, Arecibo, PR 00612-8346
[8] Columbia Astrophysics Laboratory, Columbia University, New York, NY 10027
[9] Max Planck Institut für Radioastronomie, Auf dem Hügel 69, D-53121 Bonn, Germany

Subsequent pulse timing measurements have determined the Shapiro delay and proper motion with greater precision (Kramer et al. 2006). There have also been long baseline interferometry measurements of parallax and proper motion (Deller et al. 2009). We have altered our analysis of the time scale variations to take advantage of these observations, and we have modeled the entire two dimensional time-frequency correlation function of the scintillations, rather than simply modeled its time scale. These changes have made it (just) possible to obtain a consistent interpretation. This provides the distance to the scattering region and the orientation of the pulsar orbit in celestial coordinates. It also provides an inclination estimate that is consistent with the Shapiro delay.

We now realize that the scattering is homogeneous over several binary orbits because the proper motion of the pulsar is low and the binary orbit remains entirely within the "scattering disc". Since the measured intensity is a summation over waves that have traveled through all possible paths through the scattering disc, it is quite homogeneous over that area, even if the underlying turbulence is not. However, from month to month, as we repeated the observations, different realizations of the plasma turbulence occupied the scattering disc. The level of turbulence was clearly non-stationary on this time scale.

2. OBSERVATIONS AND REDUCTION TO DYNAMIC SPECTRA

Observations of the double pulsar system were made specifically for this project with the 100-m Robert C. Byrd Green Bank Telescope (GBT) at intervals of 1-2 months from July 2004 to July 2005. All the observations were made with the SPIGOT auto-correlation spectrometer, summing the polarizations every 81.92 μs (Kaplan et al. 2005). On twelve of the epochs, observations were made with 1024 frequency channels over an 800 MHz bandwidth centered near 1900 MHz, however only 600 MHz of the bandwidth was sufficiently free of radio frequency interference (RFI) to be useful. We have also been able to analyze data taken primarily for timing at 820 MHz with 1024 channels over a 50 MHz bandwidth on five epochs, the first of which was analyzed in Paper 1. In total new and older observations span about 18 months (see Table 1 for dates). We also analyzed 1400 MHz dynamic spectra recorded earlier at Parkes (Manchester et al. 2005; Burgay et al. 2005).

The first step in the analysis of these data was to create dynamic spectra for each pulsar in each frequency band. We edited the raw SPIGOT data files for RFI and Fourier transformed the correlations with the Van Vleck corrections. With SIGPROC we formed full pulse profiles at each frequency with 64 and 256 phase bins, respectively, for pulsars A and B. Individual frequency channels were shifted with respect to each other using a dispersion measure of 48.9 cm^{-3} pc (Lyne et al. 2004). These were added to create profiles at intervals of 10 s at 1900 MHz and 5 s or 10 s at 820 MHz. The pulse intensity from each profile was estimated by first subtracting the average in an off-pulse window and then integrating the profile to create a dynamic spectrum of pulse intensity versus frequency and time. We estimated the gain in the passband using both the mean and rms in each frequency channel. We found substantial variation in both measures over the relatively broad bandwidths used. The rms appeared to be the better measure as it was less affected by RFI, which was a serious problem at 1900 MHz. Accordingly we corrected the gain of each channel by dividing it by the rms in that channel.

Figure 1 shows the dynamic spectra of the A pulsar at 1900 MHz on MJD 53560 (top) and 820 MHz on MJD 53467 (bottom). The upper panel shows the mottled structure of ISS with islands of high intensity (scintles) whose typical timescale varies from a few samples up to tens of samples, repeating over the orbital period of 147 min. This observation should be interpreted as the motion of the line of sight through a quasi-stationary spatial pattern as the pulsar and the Earth move in their orbits and the IISM drifts in a linear fashion. The time variation is determined by the spatial structure and the velocity of the line of sight. The frequency correlation is only a few samples wide and does not vary over the orbit, as discussed in §3.1.

The lower panel shows 2.5 orbital periods at 820 MHz. There is minimal RFI in this band and the eclipse by the B pulsar can be seen as thin vertical lines of low intensities near 142 and 289 min. One can see that the ISS time scale is significantly shorter and the bandwidth is much narrower, as expected for stronger scattering at the lower frequency. There are many more scintles in this dynamic spectrum. This property and the absence of RFI make the analysis of the 820 MHz observations more satisfactory than the 1900 MHz observations. Sloping features, which are obvious in both plots, change sign over the orbital period. These are due to frequency dependent refraction as we discuss in §4.

The dynamic spectra at 1900 MHz were often contaminated by RFI. The full 800 MHz bandwidth was reduced to 600 MHz because of nearly continuous RFI in the remainder of the band. In other cases RFI was short-lived and we flagged regions of the dynamic spectra where RFI was suspected and carried that flag array through subsequent processing. Flagged data was simply excluded from all subsequent analysis. In Figure 1 the flagged data were clipped at $\pm 3\sigma$ for plotting only.

3. CHARACTERIZATION AND MODELLING OF THE SCINTILLATION

In many early ISS studies the dynamic spectrum was characterized by only two parameters - the characteristic widths in time and frequency. These were usually estimated from auto-covariance functions (acfs) versus time and frequency, in each case averaged over the other coordinate. More generally the acf can be computed in two dimensions with cuts along the two axes providing time and frequency widths. Recently observers have analyzed the secondary spectrum, which is the (2-dim) Fourier transform of the acf (Stinebring et al. 2001). For nearby strong young pulsars with highly anisotropic scattering these secondary spectra show a wealth of interesting information in the form of parabolic arcs. The secondary spectra of pulsar A do show parabolic arcs, but they are not sufficiently well-defined to assist with our analysis. However we have found the 2-dim acf very useful in estimating both the anisotropy of the spatial structure and the mean phase gradient over the scattering disc. This is discussed in detail in section §4.

A theoretical model for the 2-dim acf $\rho_I(\tau, \nu)$ is devel-

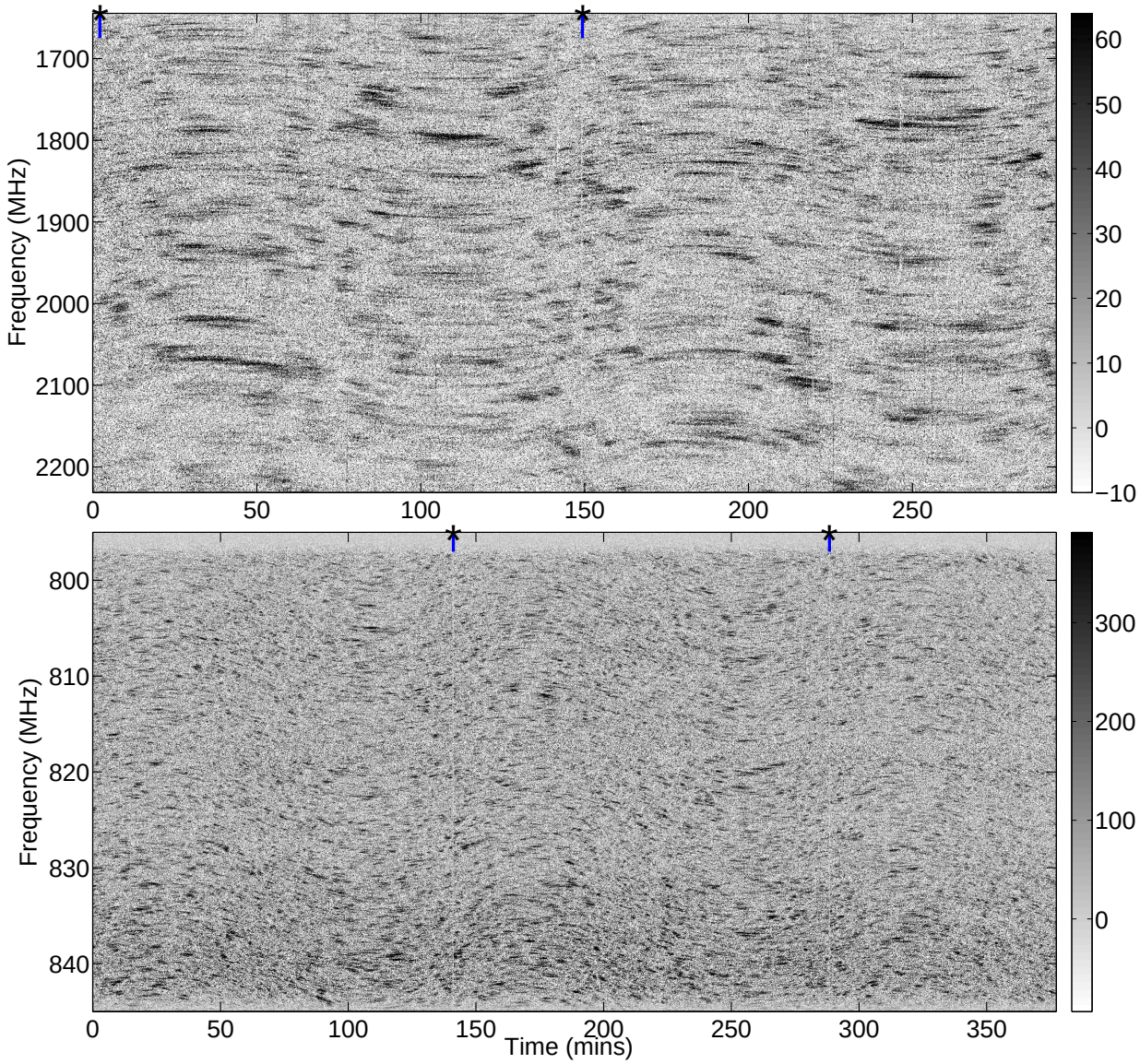

Figure 1. Dynamic spectra of the A pulsar taken at the Green Bank Telescope in 1024 channels at 10 s intervals. *Upper:* MJD 53560 at 1900 MHz. *Lower:* MJD 53467 at 820 MHz. The total durations differ and a short line with a * on the top axis marks the time of A's eclipses.

oped in the Appendix. It is actually a "cut" through a 3-dim acf $\rho_I(\vec{r} = \vec{V}\tau, \nu)$ where $\vec{V}$ is the velocity of the line of sight through the IISM and $\vec{r}$ is the transverse coordinate. Thus the apparent time scale is the spatial scale in the direction of $\vec{V}$ divided by the speed. The width in frequency is inversely proportional to the rms scattering angle and thus to the strength of scattering. Here, as we want to study how the time and frequency scales of pulsar A vary over its orbit, we have computed the 2-dim acf from short blocks of the dynamic spectrum, (which must be long enough to include at least one ISS timescale). An example is shown in the upper panel of Figure 2 for the data from MJD 53560 shown in Figure 1; the lower panel is a best-fit theoretical model which we discuss in section §4.

3.1. *ISS Characteristics and Model*

The characteristic scales in frequency and time have been defined by where the auto-correlation functions fall to 0.5 and e^{-1}, respectively and we will adhere to this convention. In our analysis we estimate these by fitting an ISS model to each acf, since the fitting makes full use of the data. In deriving the model we assume the scintillations are dominated by scattering from a thin region a distance z_0 from the observer. The electron density fluctuations in the screen are described by a Kolmogorov wavenumber spectrum which is homogeneous, at least over the scattering disc. The pulsar is at a distance of z_p from the observer and the fractional distance from the pulsar to the screen is $s = (z_p - z_0)/z_p$. Note that this thin scattering region can dominate the scattering, which is a path integral over density squared, but may not dominate the dispersion, which is a path integral over density. We also assume that refractive variations are negligible over the scales of interest, i.e. the scintillations are in

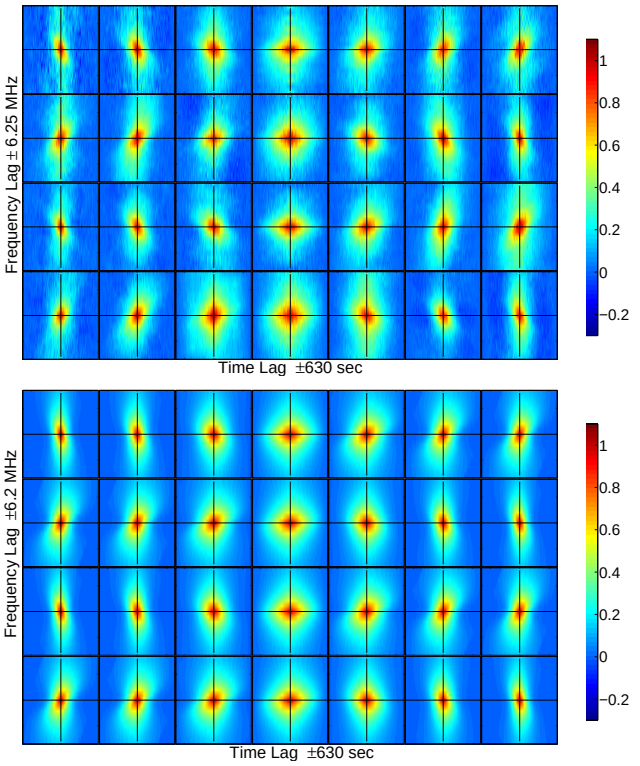

Figure 2. Frequency-time acfs for the dynamic spectrum in the top panel of figure 1 (at 1900 MHz on MJD 53560). *Upper* Observed; *Lower* Model. Two complete orbital periods are shown, each divided into 14 blocks of 630s. Time advances left to right and top to bottom. The acfs are normalized by the variance of the ISS. The noise spike at the origin is suppressed by the color table which saturates in dark red at unity. Note the changing width in time lag, the nearly constant width in frequency lag and repeating patterns of positive and negative slope.

the diffractive limit. This model is the starting point for many studies of ISS, which have been used to investigate fine-scale turbulence in the interstellar plasma (Armstrong et al. 1995; Cordes & Lazio 2005). These studies assumed an isotropic density spectrum, but as recent observations such as Brisken et al. (2010) have shown evidence for anisotropy, we also include it here.

Propagation through such a layer causes a phase modulation which is usefully characterized by the phase structure function $D_\phi(\boldsymbol{\sigma}) = \langle(\phi_p(\boldsymbol{r}) - \phi_p(\boldsymbol{r}+\boldsymbol{\sigma}))^2\rangle$, where $\phi_p(\boldsymbol{r})$ is the plasma phase contribution at transverse coordinate $\boldsymbol{r}$. The electric field correlation at the output of the phase screen is $\Gamma_E(\boldsymbol{\sigma}) = \exp(-0.5 D_\phi(\boldsymbol{\sigma}))$, and it is invariant with distance.

We describe the anisotropy by two quantities, the axial ratio A_R and the orientation of the major axis ψ_{AR} of the inhomogeneities in the plasma density. In terms of the major (σ_{maj}) and minor axes (σ_{min}) the structure function can then be written

$$D_\phi(\boldsymbol{\sigma}) = \Big(\frac{\sigma_{maj}^2}{s_0^2 A_R} + \frac{A_R \sigma_{min}^2}{s_0^2}\Big)^{5/6}. \qquad (1)$$

In rotated coordinates (σ_x, σ_y) the quadratic form becomes

$$D_\phi(\boldsymbol{\sigma}) = Q(\boldsymbol{\sigma})^{5/6} s_0^{-5/3}\ ,$$
$$Q(\boldsymbol{\sigma}) = a\sigma_x^2 + b\sigma_y^2 + c\sigma_x\sigma_y\ , \qquad (2)$$

with the major axis rotated by ψ_{AR} clockwise from the x-axis. The mean diffractive scale s_0 decreases as the strength of scattering increases. In this work we find it convenient to define anisotropy in terms of the bounded parameter R,

$$R = (A_R^2 - 1)/(A_R^2 + 1) \qquad (3)$$

which lies in the range 0 to 1. The coefficients of the quadratic form Q become:

$$a = [1 - R\cos(2\psi_{AR})]/\sqrt{1-R^2}$$
$$b = [1 + R\cos(2\psi_{AR})]/\sqrt{1-R^2} \qquad (4)$$
$$c = -2R\sin(2\psi_{AR})/\sqrt{1-R^2}$$

In the diffractive scintillation limit the spatial correlation function for intensity is $C_I(\boldsymbol{\sigma}) = |\Gamma_E(\boldsymbol{\sigma})|^2$ at the Earth. There are no intensity fluctuations at the output of the screen. The temporal correlation function at the Earth is $C_I(\tau) = \exp(-D_\phi(\boldsymbol{V_{los}}\tau))$, where $\boldsymbol{V_{los}} = (1-s)\boldsymbol{V_{PA}} + s\boldsymbol{V_E} - \boldsymbol{V_{IS}}$ is the transverse velocity of the "line of sight" with respect to the plasma. Here V_E, V_{IS} and V_{PA} are the velocities of the Earth, the plasma, and pulsar A respectively (Cordes & Rickett 1998), all defined with respect to the Sun.

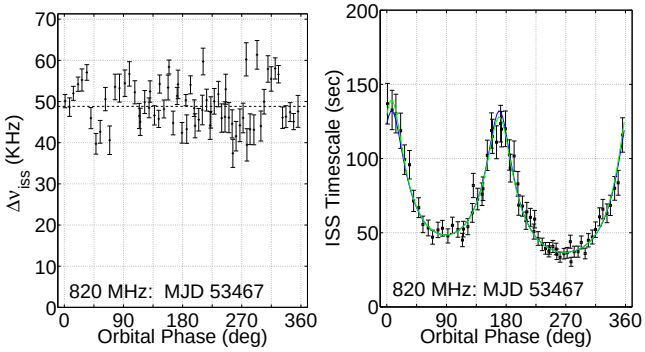

Figure 3. Frequency $\Delta\nu_{iss}$ (left) and Time $T_{\rm ISS}$ (right) scales for the dynamic spectrum shown in the lower panel of Figure 1 versus true anomaly orbital phase ϕ, as defined in §3.2. The channel bandwidth is indicated by the dashed line in the left panel. The theoretical best fit model is overplotted in the right panel. The error bars are $\pm 1\sigma$.

The acf versus frequency in the diffractive limit is more complex (Lovelace 1970). It involves a Fourier-like integral which was solved by Armstrong & Rickett (1981) for the case of an isotropic Kolmogorov spectrum. Here we have done this integral numerically for the anisotropic model and fitted it to the acf of each block in each observing epoch. From this fit we obtain the parameters $\Delta\nu_{iss}$ and $T_{\rm ISS}$ as a function of orbital phase ϕ. Details are given in Appendix A. The two scales $\Delta\nu_{iss}(\phi)$ and $T_{\rm ISS}(\phi)$ are plotted in Figure 3 for the 820 MHz dynamic spectra shown in the lower panel of Figure 1. The model predicts that $\Delta\nu_{iss}$ should be independent of the pulsar velocity and indeed there is no discernible correlation with ϕ, however there is considerably more scatter in the estimates from each block than the fitting errors, as discussed by Coles et al. (2010). As $\Delta\nu_{iss}$ is comparable to the channel bandwidth, we have barely resolved the ISS in frequency. As expected $T_{\rm ISS}$ varies strongly

over the binary orbit, primarily because of the variation in the pulsar velocity.

The error bars on $T_{\rm ISS}$ are the formal standard errors of the fit of a covariance model to the measured covariance. Most of the variance is due to white noise, so the error bars have not been corrected for the correlation between measured covariance points. These error bars are used in a subsequent weighted fit; however, the error estimates resulting from this subsequent fit are independent of the scaling of the errors in $T_{\rm ISS}$.[10]

3.2. *ISS Timescale Variation over the Pulsar Orbit*

The timescale $T_{\rm ISS}$ is easily determined in the isotropic case ($A_R = 1$, $R = 0$), to be $T_{\rm ISS} = s_0/V_{los}$. In the general case one must solve $\exp[-D_\phi(\boldsymbol{V_{los}}T_{\rm ISS})] = 1/e$ for $T_{\rm ISS}$:

$$(1/T_{\rm ISS})^2 = Q(\mathbf{V_{los}})/s_0^2\,, \tag{5}$$

so here too $T_{\rm ISS}$ depends inversely on V_{los}.

In our case pulsar A is in a binary system so that $\boldsymbol{V_{PA}}$ is the sum of the binary center of mass velocity $\boldsymbol{V_P}$ and A's orbital velocity $\boldsymbol{V_{oA}}$ about the center of mass, which have been measured accurately from pulsar timing (Kramer et al. 2006). It is the effect of the varying orbital velocity that is responsible for the variation in $T_{\rm ISS}(\phi)$ over the orbital period in Figure 3. We can then fit a model to $T_{\rm ISS}(\phi)$ and use the known $\boldsymbol{V_{oA}}$ to calibrate a model for the other variables (s_0, s, and $\boldsymbol{V_{IS}}$). This was first proposed by Lyne (1984) and used by Ord et al. (2002) and Ransom et al. (2004) under isotropic scattering and generalized to anisotropic scattering in paper 1. The technique is most valuable for short period binaries because the orbit lies entirely within the scattering disc and a homogeneous scattering model fits the observations over a few orbits very well. We will show that the time series $T_{\rm ISS}(\phi)$ possesses 5 degrees of freedom and one could expect, in an isotropic plasma, to determine the scattering variables listed above and also the orbital inclination i. When the plasma is anisotropic there are two more unknowns in A_R and ψ_{AR} and a complete solution requires more information.

As the orbital velocity of the pulsar is the reference, we use equation 5 in the pulsar frame where the spatial scale is $s_p = s_0/(1-s)$. The appropriate "scintillation velocity" is then $\boldsymbol{V_A} = \boldsymbol{V_{los}}/(1-s) = \boldsymbol{V_C} + \boldsymbol{V_{oA}}$, where

$$\boldsymbol{V_C} = \boldsymbol{V_P} + \boldsymbol{V_E}s/(1-s) - \boldsymbol{V_{IS}}/(1-s) \tag{6}$$

which is constant during an observation, but obviously varies over the year. We can write the transverse scintillation velocity of A $\boldsymbol{V_A}$, in terms of $\boldsymbol{V_C}$ and its true anomaly θ and its orbital phase from the line of nodes $\phi = \omega + \theta$, where ω is the longitude of periastron, as follows:

$$\begin{aligned} V_{Ax} &= V_{\rm Cx} + V_o[e\sin\theta\cos\phi - (1+e\cos\theta)\sin\phi] \\ &= V_{\rm Cx} - V_o e\sin\omega - V_o\sin\phi \\ V_{Ay} &= V_{\rm Cy} + \cos i[V_o e\sin\theta\sin\phi + V_o(1+e\cos\theta)\cos\phi] \\ &= V_{\rm Cy} + \cos i(V_o e\cos\omega + V_o\cos\phi). \end{aligned} \tag{7}$$

Here (V_{Ax}, V_{Ay}) is in agreement with the equations given by Ord et al. (2002), but differs from equations (4) and (5) of Bogdanov et al. (2002). Here V_o is a mean orbital velocity given by $V_o = 2\pi a/(P_{\rm b}\sqrt{1-e^2})$ in terms of P_b the period, a the semi-major axis of A and e the eccentricity of the orbit. We define the inclination i as the angle between the orbital angular momentum $\mathbf{l}$ and the direction from the Earth toward the center of mass $\hat{\mathbf{s}}$. We choose the x-coordinate along the line of nodes ($\hat{\mathbf{x}} = \hat{\mathbf{s}} \times \hat{\mathbf{l}}/\sin i$ and $\hat{\mathbf{y}} = \hat{\mathbf{s}} \times \hat{\mathbf{x}}$), which with an inclination near 90° would make the angular momentum nearly anti-parallel to the y-axis.

We rewrite equation 5 in the pulsar frame and model the data $T_{\rm ISS}(\phi)$ by:

$$\begin{aligned} (1/T_{\rm ISS})^2 &= Q(\mathbf{V_A})/s_p^2 \\ &= (aV_{Ax}^2 + bV_{Ay}^2 + cV_{Ax}V_{Ay})/s_p^2. \end{aligned} \tag{8}$$

When the velocities from equation (7) are substituted into equation (8) we obtain the expression as a sum of five harmonics.

$$\begin{aligned} (1/T_{\rm ISS}(\phi))^2 = K_0 &+ K_S\sin\phi + K_C\cos\phi \\ &+ K_{S2}\sin 2\phi + K_{C2}\cos 2\phi, \end{aligned} \tag{9}$$

where the harmonic coefficients are shown below.

$$\begin{aligned} K_0 &= [0.5V_o^2(a + b\cos^2 i) + a(V_{\rm Cx} - V_o e\sin\omega)^2 \\ &\quad + b(V_{\rm Cy} + V_o e\cos\omega\cos i)^2 + \\ &\quad c(V_{\rm Cx} - V_o e\sin\omega)(V_{\rm Cy} + V_o e\cos\omega\cos i)]/s_p^2 \\ K_S &= -V_o[2a(V_{\rm Cx} - V_o e\sin\omega) \\ &\quad + c(V_{\rm Cy} + V_o e\cos i\cos\omega)]/s_p^2 \\ K_C &= V_o\cos i[c(V_{\rm Cx} - V_o e\sin\omega) \\ &\quad + 2b(V_{\rm Cy} + V_o e\cos i\cos\omega)]/s_p^2 \\ K_{S2} &= -0.5cV_o^2\cos i/s_p^2 \\ K_{C2} &= 0.5V_o^2(-a + b\cos^2 i)/s_p^2 \end{aligned} \tag{10}$$

These 5 harmonics carry all the information in the data set, i.e. they are "sufficient statistics" for the ISS with a general (eccentric) orbit.

The IISM can be characterized by five quantities ($V_{\rm Cx}, V_{\rm Cy}$, s_0, R and ψ_{AR}), so that the 5 measurable parameters are insufficient to determine all the IISM parameters and i unless R is known to be zero. Further, the double pulsar is nearly edge-on so K_{S2} and K_C are small and the signal to noise ratio is marginal. One could still solve for $s_0, V_{\rm Cx}$, and $V_{\rm Cy}$ if R and ψ_{AR} were known. But since the ISS anisotropy is not known, extra information is needed as discussed in §3.3. Thus we estimate the five harmonic coefficients as a first step in extracting the full IISM parameter set and the inclination of the orbit.

In estimating $T_{\rm ISS}$ we split the dynamic spectrum of A into time blocks of length 310 or 630 s, subtracted the mean from each channel, and computed the temporal autocorrelation function $\rho(t)$ of each block averaged over all channels. We fitted a theoretical model to the autocorrelation of each block beginning at the first non-zero time lag to avoid the "noise spike". We used the theoretical form for diffractive ISS from a Kolmogorov scattering medium $\rho(t) = \exp[-(t/T_{\rm ISS})^{5/3}]$. Since the time resolution in the dynamic spectrum is 5 or 10 sec we convolved the model acf with the appropriate triangular resolution function. Also, since the block autocorrelation estimates

[10] Errors are 1 standard deviation throughout unless defined otherwise

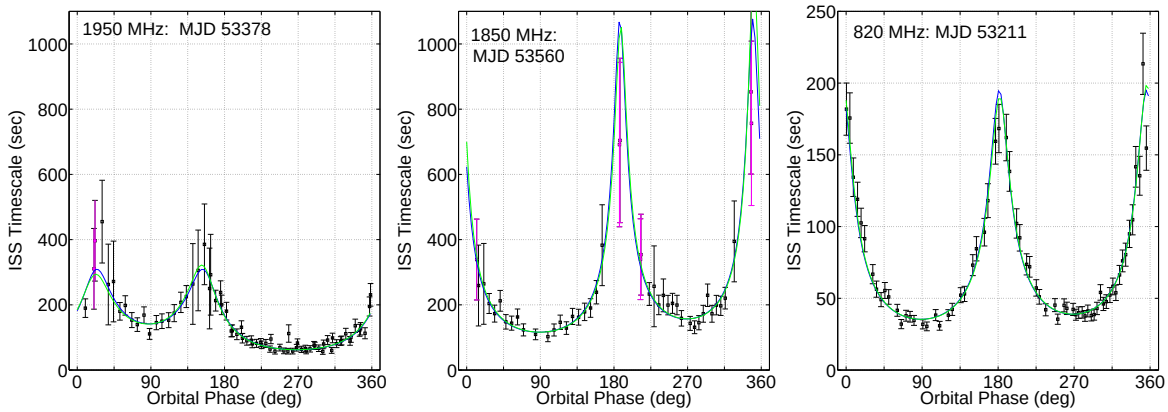

Figure 4. Plots of $T_{\rm ISS}(\phi)$ versus true anomaly orbital phase ϕ at 1900 MHz (*left to right*) from MJD 53378 & 53560 and 820 MHz from MJD 53211. Data are open symbols with error bars (magenta for the longer blocks). The 3 (5) parameter fits are blue (green) lines.

are weighted with a triangle function, we applied that same triangle weight to the model before fitting.

In choosing the block length there is a trade-off between the need for short block lengths, since the time scale is continuously changing, and the need to keep the block length longer than the time scale. At 820 MHz $T_{\rm ISS}$ was always shorter than 310 s, and so we we fixed the blocks at that length. However, at 1900 MHz the diffractive scintillation scale is larger and hence the longest time scales are sometimes greater than 310 s. So at the higher frequency we computed $T_{\rm ISS}$ for blocks of both 310 s and 630 s (1/14th of the orbital period). We then selected the estimates from the shorter blocks except where the longer block estimate gave $T_{\rm ISS} > 310$ s; in which case we replaced the two nearest shorter blocks by the single block of 630 s. We note that when $T_{\rm ISS}$ is large, it is quite sensitive to the form of the correlation function used in the model and is accompanied by larger errors. This makes it difficult to exploit the fact that near the times of slow ISS the scintillation velocity vector rotates rapidly and so has the potential to determine the anisotropy of the ISS. At 1900 MHz we omitted the occasional blocks which were contaminated by RFI in all channels.

We then fitted the five harmonic model versus orbital phase (ϕ) to the estimates of $T_{\rm ISS}$ from each block. Since equation (9) is linear in the 5 harmonic coefficients, we started by fitting to $T_{\rm ISS}(\phi)^{-2}$, directly. However, for a weighted fit we need errors in $T_{\rm ISS}^{-2}$, which could not be reliably obtained from the error ($\sigma_{T_{\rm ISS}}$) estimated for each $T_{\rm ISS}$. So we used the reciprocal of the square root of that equation to model $T_{\rm ISS}(\phi)$, after first smoothing it over the range of phases in each block. We performed a non-linear least squares fit with residuals weighted by $1/\sigma_{T_{\rm ISS}}$ starting from the model parameters of the $T_{\rm ISS}^{-2}$ fit. The fits for the 5 coefficients and their standard errors are listed in Table 1. As expected the coefficients K_C and K_{S2} are small for all epochs. Examples of the fits are shown in figure 4. The blue lines show fits with only 3 harmonic coefficients ($K_C = 0, K_{S2} = 0$) assuming $\cos i = 0$, which are barely distinguishable from the fits with 5 coefficients.

3.3. *Annual Modulation by the Earth's Motion*

3.3.1. *Analysis overview*

In Paper 1 we analyzed the observed variation in $T_{\rm ISS}$ over orbital phase at a single epoch and found that any anisotropy in the ISS pattern has a strong affect on the estimate of the system velocity. We also observed partial correlation in the ISS of the two pulsars. In combination the observations could be fitted by any anisotropy $R > 0.8$ which corresponded to a very wide range of system velocities. By assuming that $0.97 \gtrsim R \gtrsim 0.8$ we constrained the system velocity to be in the range 51 to 81 km s^{-1}, lower than 140 km s^{-1} if $R = 0$. However the analysis did not correct for the effects of the changing velocity of the Earth and any (unknown) velocity of the interstellar scattering region. Subsequent pulsar timing and VLBI observations of the system proper motion and parallax yielded a system velocity $\lesssim$20 km s^{-1}. In the observations reported here we use observations over 18 months to resolve these difficulties.

As noted in the previous section, our $T_{\rm ISS}(\phi)$ observations have been quantified by the 5 orbital harmonic coefficients measured at each epoch over the course of 18 months. Our goal now is to fit a model to these coefficients assuming that the plasma parameters are constant over this period. By including the (known) Earth's velocity we add two new unknowns, the location of the screen s and the angle Ω defined CCW from celestial North through East to the x-axis of the pulsar orbit.

Table 1
The five orbital harmonic coefficients versus date. The first 5 lines are 820 MHz and the latter 12 lines are at 1900 MHz. The units are 10^{-4} sec^{-2}. Day = MJD-53000.

Day	K_0	K_s	K_c	K_{s2}	K_{c2}
−3	3.46±.06	−2.63±.08	−0.10±.03	0.10±.05	−2.77±.06
211	3.79±.10	0.70±.11	−0.02±.02	−0.06±.07	−3.51±.10
311	4.76±.13	−3.63±.16	−0.15±.05	0.17±.08	−4.02±.12
379	6.19±.14	−6.74±.19	−0.04±.07	0.04±.08	−4.40±.12
467	3.25±.08	−1.57±.10	−0.05±.03	0.01±.06	−2.57±.08
202	0.96±.09	0.41±.15	0.12±.12	−0.10±.09	−1.07±.12
203	0.89±.05	0.29±.07	0.00±.01	0.04±.04	−0.86±.05
274	0.92±.06	−0.40±.08	0.03±.02	−0.06±.04	−0.84±.06
312	1.35±.06	−1.23±.07	−0.04±.02	0.04±.03	−1.15±.06
319	1.41±.05	−1.39±.07	−0.06±.03	0.05±.04	−1.13±.05
374	0.91±.05	−1.02±.09	−0.02±.04	0.03±.05	−0.59±.06
378	0.94±.03	−1.05±.05	−0.02±.02	0.02±.03	−0.62±.03
415	0.74±.04	−0.80±.06	−0.00±.03	0.02±.04	−0.53±.04
451	0.84±.03	−0.71±.05	−0.02±.02	0.05±.03	−0.67±.04
462	0.74±.02	−0.60±.03	−0.04±.01	0.04±.02	−0.58±.02
505	0.54±.03	0.06±.04	−0.00±.01	0.01±.03	−0.49±.04
560	0.29±.01	0.16±.02	−0.00±.00	−0.01±.01	−0.26±.01

However the extra information in the annual variation can, in principle, be used to estimate the anisotropy. As the Earth's velocity provides an annual sinusoidal variation, the responses of the 5 orbital harmonics also show annual and semiannual harmonics though they are correlated. The annual-harmonics of the three strongest orbital-harmonics K_{C2}, K_S and K_0 provide 7 degrees of freedom and those of the two weaker orbital-harmonics K_{S2} and K_C add two more for a total of 9. Thus we can hope to estimate the five IISM quantities ($V_{\rm Cx}, V_{\rm Cy}$, s_0, R and ψ_{AR}), plus s, Ω and $\cos i$.

We have found that we can obtain independent estimates of the anisotropy at each epoch by fitting the entire frequency-time acf, ($\rho_I(\tau,\nu)$) rather than just the time scale, but this can only be done for six of the best dynamic spectra, including all five observations at 820 MHz. The process is complicated by the need to also fit for a transverse gradient in the interstellar phase, because the phase gradient causes a first-order effect on ρ_I off the time axis. This process is discussed in section §4. The result is that we are able to estimate the five IISM parameters plus the phase gradient at each of these six epochs. This is very useful in searching for time variations in parameters otherwise assumed to be constant.

Accordingly we use a hybrid procedure. First we assume $\cos i = 0$ and fit the annual variation of the three strong orbital harmonics. From this we can estimate the five IISM parameter plus s and Ω. Second we include $\cos i$ in the parameters and add the two weaker orbital harmonics to the data to be fit. This provides an estimate of $\cos i$ and also improves the estimate of the anisotropy. Then we fit the frequency-time acfs for the 6 best dynamic spectra and obtain estimates of the time variation of the IISM parameters. Finally we include these time variations in the fit of the annual variation of the five orbital harmonics.

Note that the hybrid analysis is necessarily a compromise. We are estimating diffractive scintillation parameters from a few hours of data at each epoch, in a situation where we expect statistical variations in these parameters on the timescale for refractive scintillations (several days). Thus the estimates are in the "snapshot" regime, as discussed by Romani et al. (1986), who give theoretical predictions for the rms variation expected for various diffractive ISS parameters such as the anisotropy, see also the simulations by Coles et al. (2010). Thus an ideal model could allow the ISS parameters to vary from one epoch to the next, as in the five observations at 820 MHz. However, there is insufficient information to include such variations in the analysis at 1900 MHz of $T_{\rm ISS}(\phi)$ and its harmonic coefficients.

3.3.2. *Non-stationarity in the Level of Turbulence*

The harmonic coefficients K_{C2} and K_{S2} are independent of V_E and should be constant over the year. Although K_{S2} is too weak to be useful in testing this hypothesis, K_{C2} is accurately measured. It is inversely proportional to the square of the spatial scale in the x-direction, i.e. s_p^2/a and to the frequency decorrelation width $\Delta\nu_{iss}$.

We found that both K_{C2} and $\Delta\nu_{iss}$ varied significantly over the 18 months of our observations. We have used K_{C2} to infer $\Delta\nu_{iss}$ and plotted both the inferred and directly measured $\Delta\nu_{iss}$ in Figure 5 (left and right panels respectively). The equation used is

$$\Delta\nu_{KC2} = \frac{-aV_0^2}{2K_{C2}} \frac{s}{1-s} \frac{2\pi\nu_m^2}{cL} \tag{11}$$

where L is the distance from the Earth to the pulsar and ν_m is the center frequency. One can see very significant variations in both, although they are not identical. The difference is most probably because they have different dependence on anisotropy. In particular only K_{C2} depends on ψ_{AR} and this parameter can vary between different realizations of the same random process.

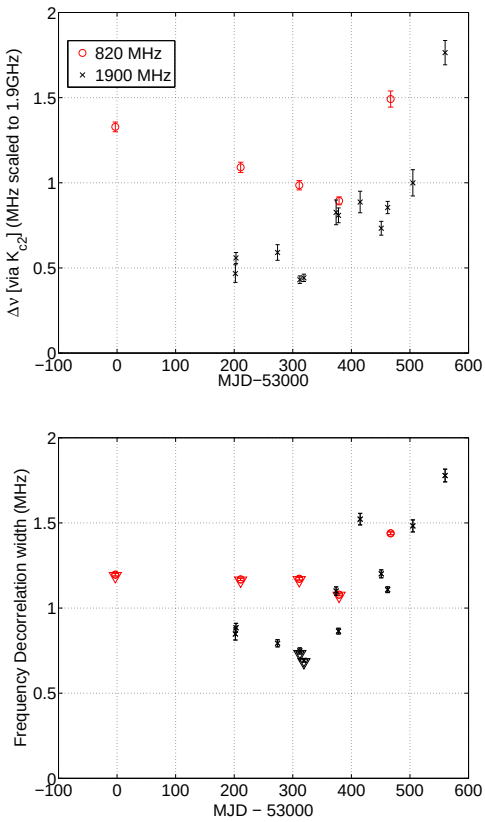

Figure 5. Strength of ISS expressed as equivalent $\Delta\nu_{iss}$ at 1.9 GHz: *Upper* Derived from K_{C2} and equation 11. *Lower* Estimated from fitting to acf (averaged over all the blocks at each epoch). Error bars derived from the scatter among the blocks at each epoch.

We can remove the effect of these changes in s_p on the other parameters by normalizing all the harmonic coefficients by K_{C2} but this will not correct for minor variations in the anisotropy. This variation in the diffractive scale s_p seems greater than expected from refractive effects, but as in other pulsar observations it may indicate that the scattering medium is not well represented as homogeneous turbulence on a time scale of weeks to months (Hemberger & Stinebring 2008). Thus we might also expect to see some variation in the anisotropy reflected in the harmonic analysis. We return to this question in §4.

3.3.3. *Annual Variation in Harmonic Coefficients*

The transverse velocity of the Earth and the proper motion of the pulsar are defined in celestial coordinates, so we rotate them by the unknown angle Ω into

(x,y) coordinates defined by the pulsar orbital plane, i.e. $\boldsymbol{V_{xy} = MV_{\alpha\delta}}$ where $\boldsymbol{M}$ is

$$\boldsymbol{M} = \begin{pmatrix} \sin\Omega & \cos\Omega \\ -\cos\Omega & \sin\Omega \end{pmatrix}. \quad (12)$$

It remains convenient to define the unknown interstellar velocity in x, y coordinates. We then substitute $\boldsymbol{V_C}$ into equation (10) and knowing the Earth's velocity obtain model equations for the harmonic coefficients at each epoch. We expect s_p to depend on the observing frequency, but we have removed its influence by normalizing the two remaining coefficients by K_{C2}, i.e. $k_s = K_S/K_{C2}$ and $k_0 = K_0/K_{C2}$. Thus we can combine the data from all frequency bands (820, 1400 and 1900 MHz) by plotting k_s and k_0 versus date in figure 6. The overlap of values from different frequencies confirms the validity of this approach.

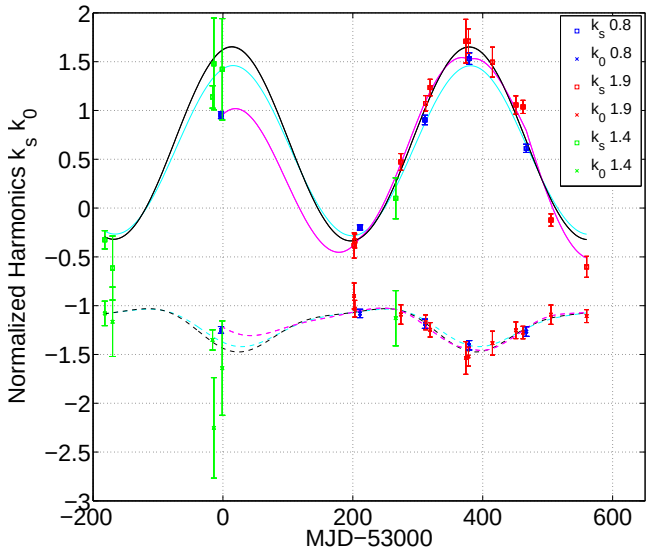

Figure 6. Normalized harmonic coefficients k_s and k_0 versus day. Symbols indicate the observing frequency in GHz. Points at 1.4 GHz were not included in the fit, since their error bars were substantially larger. Three models are shown as solid lines for k_s and dashed lines for k_0; the cyan lines are constant velocity fits including the point at day -3; the black lines are the same but excluding day -3. The magenta lines include day -3 but are fitted with variable velocity as discussed in section 4.

The equations for the two normalized coefficients versus date now involve $\boldsymbol{V_C}$, R, ψ_{AB}, s, and Ω, but it is convenient to group them into the following three combinations:

$$\begin{aligned} u_x &= (V_{\rm Cx} - eV_o \sin\omega)/V_o \ , \\ u_y &= \sqrt{b/a}(V_{\rm Cy} + eV_o \cos i \cos\omega)/V_o \\ w &= c/\sqrt{ab} \end{aligned} \quad (13)$$

then we have

$$\begin{aligned} k_s &= 4u_x + 2wu_y; \\ k_0 &= -1 - 2u_x^2 - 2wu_xu_y - 2u_y^2 \ . \end{aligned} \quad (14)$$

One can see that k_s is linear in velocity, whereas k_0 is quadratic. The known sinusoidal variation in V_E will appear in k_s scaled by $s/(1-s)$ and shifted in phase due to the rotation of coordinates by Ω. So the annual variation of k_s has three degrees of freedom (including the constant). The additional information provided by k_0 is the square of a known sine wave plus an unknown constant. The semiannual harmonic will provide an estimate of the axial ratio and the annual an estimate of V_{ISy}. Thus including the constant term and K_{C2} there are 7 degrees of freedom in total. This is sufficient to estimate s_0, s, Ω, $\boldsymbol{V_{IS}}$, R and ψ_{AR}. The remaining two coefficients, k_{s2} and k_c are highly correlated and add only two degrees of freedom. However, with ω and/or e known from timing one can estimate $\cos i$.

In terms of the physical parameters we have:

$$u_x = p_1 + p_2 V_{Ex} \ \ ; \ \ u_y = p_3 + p_4 V_{Ey}, \quad (15)$$

where

$$\begin{aligned} p_1 &= [V_{Px} - V_{ISx}/(1-s) - eV_o \sin\omega]/V_o \\ p_2 &= s/[V_o(1-s)] \\ p_3 &= \sqrt{b/a}[V_{Py} - V_{ISy}/(1-s) + eV_o \cos i \cos\omega]/V_o \\ p_4 &= p_2\ \sqrt{b/a}. \end{aligned}$$

In fitting the model we use the parameters obtained from the pulsar timing solution of Kramer et al. (2006) for eccentricity e and for the longitude of periastron ω as a function of date; for the proper motion velocity we use: $V_{\rm P\alpha} = -17.8$, $V_{\rm P\delta} = 11.6$ km s^{-1} from Deller et al. (2009). This depends on the VLBI parallax distance of $1.15^{+.22}_{-.16}$ kpc to the pulsar, which is larger than 0.5 kpc based on the Cordes & Lazio (2005) Galactic electron model. This smaller distance and the most recent proper motion estimated from pulse timing (Kramer private communication 2014) give a slower pulsar proper motion velocity: $V_{\rm P\alpha} = -5.3$, $V_{\rm P\delta} = 6.2$ km s^{-1}. In §4.1 we discuss the small effect of using this lower pulsar velocity.

We initially optimized all 6 physical parameters s, Ω, $\boldsymbol{V_{IS}}$, R and ψ_{AR} (under the assumption that $\cos i = 0$) to fit the data for k_s and k_0 at 820 and 1900 MHz. The result is shown in Figure 6 by a cyan line. This fit has a high reduced $\chi^2 \sim 9$, largely due to the obvious outlier at day -3 (MJD 52997). This is an 820 MHz observation with very small error bars but it is obviously discrepant because it does not agree with a similar observation one year later. The dynamic spectrum for these data were at 5 s intervals, in contrast to all the others which used 10 s intervals. Though this would change the pulse intensity and could influence $T_{\rm ISS}$, it should not distort the estimation of the harmonic coefficients in $T_{\rm ISS}$. It suggests an error in our assumptions that the velocity and anisotropy of the IISM were constant over this period, so we continued the analysis with the data point at MJD 52997 excluded. The results are shown as a blue line in Figure 6 and tabulated in the first column of Table 2. The χ^2 is reduced to a more reasonable 2.6, but the errors on the velocity and the anisotropy are high. We conclude that the location of the scattering medium s is quite accurately estimated, the orientation of the pulsar orbit in celestial coordinates Ω is adequately determined, but the parameters of the IISM are weakly constrained.

3.3.4. *Constraining the orbital inclination and scattering anisotropy*

In view of the difficulties in fitting a fixed set of parameters to k_s, k_0 and with the hope of determining the sign of $\cos i$, we tried fitting all four normalized harmonic coefficients with $\cos i$ restricted to $i = 88.7°$ or $91.3°$. The measured Shapiro delay (Kramer et al. 2006) provides estimates of $\sin i$, leaving an ambiguity in the sign of $\cos i$, bounded by $|\cos i| = 0.023^{+.013}_{-.009}$. The observed harmonics k_c, k_{s2} are plotted Figure 7 versus date and the best fit models for these two inclinations are over plotted. Even with the relatively large errors in these coefficients, it is clear that the solid curves for $i = 88.7°$ fit better than the dashed curves for $i = 91.3°$. These two fits are tabulated in the third and fourth columns of Table 2. It is remarkable how much the inclusion of the fit for $\cos i$ and the two extra harmonics improved the error bars on all the fitted parameters. The results for $i = 91.3°$ have a higher χ^2, the parameters do not match those of the two harmonic fit well, and the IISM velocities are well outside of the expected range. We conclude that the location of the screen and the orientation of the orbital plane are now accurately estimated, and the estimates of the anisotropy and velocity of the IISM are now useful. Encouraged by this result we included $\cos i$ as a fitted parameter, obtaining $i = 88.6 \pm 0.4°$.

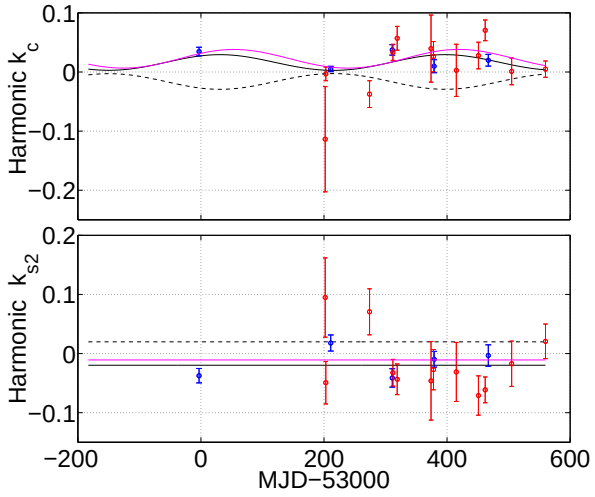

Figure 7. Normalized harmonic coefficients k_c and k_{s2} versus day (blue 820 MHz and red 1900 MHz). Models were fit to all 4 harmonic coefficients, excluding those on day -3. The solid black curves are constant velocity models with $i = 88.7°$ and the dashed black curves are the same with $i = 91.3°$. The magenta curve is from a variable velocity fit discussed in section 4.

To show the improvement in fitting four harmonics we redo the three fits discussed, i.e. the fit for two harmonics with $\cos i = 0$ and the fits for four harmonics with $\cos i = \pm 0.023$. Here we step R and $2\psi_{AR}$ over the ranges: $0 \le R \le 1$; $0 \le 2\psi_{AR} \le 2\pi$ while fitting for the other 4 parameters at each grid point. The left panel of figure 8 shows the sum of the squares of the residuals as a polar plot in this space, which could be called a Poincaré circle; see also a similar plot by Grall et al. (1997).

The left panel shows the result for the two harmonic fit with $i = 90°$. The mean squared error surface is very broad, covering the left half of the Poincaré circle. The middle panel is for a four harmonic fit with $i = 88.7°$. It is much more compact, but consistent with the left panel. The right panel is for a four harmonic fit with

Table 2
Parameters estimated from fitting to annual variation of the normalized orbital harmonic coefficients at 0.8 & 1.9 GHz, excluding MJD 52997. The first column is a two harmonic fit, the others are four harmonic fits.

Parameter	$i = 90°$	$i = 91.3°$	$i = 88.7°$
s	0.71 ± 0.03	$0.70 \pm .02$	0.70 ± 0.02
Ω (deg)	69 ± 31	111 ± 8	61 ± 8
R	$0.76 \pm .27$	$0.96 \pm .11$	0.71 ± 0.21
ψ_{AR} (deg)	72 ± 36	118 ± 8	61 ± 9
V_{ISx} (km s^{-1})	-12 ± 29	-79 ± 68	-9 ± 11
V_{ISy} (km s^{-1})	50 ± 32	≥ 100	42 ± 22
$N_{\rm dof}$	26	58	58
Reduced χ^2	2.6	3.2	2.8

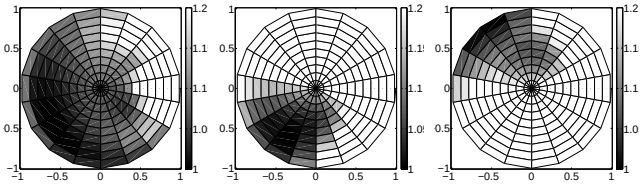

Figure 8. Residuals (χ^2) from fitting harmonic coefficients versus date (excluding MJD 52997) in a "Poincaré" polar plot of anisotropy (R, $2\psi_{AR}$). Residuals are normalized to the global minimum. *Left:* Fitting 2 coefficients k_s, k_0. *Center* Fitting 4 coefficients k_s, k_0, k_c, k_{s2} with $i = 88.7°$. *Right* Fitting 4 coefficients k_s, k_0, k_c, k_{s2} with $i = 91.3°$. Looking toward the pulsars their orbit line of nodes (x-axis) is to the right in the plot. The orientation of the major axis (ψ_{AR}) is defined clockwise from x.

$i = 91.3°$. It is completely disjoint with the other panels, and shows a much higher axial ratio. We conclude that $\cos i > 0$ and that the six parameters are reasonably well constrained.

The fit is not completely satisfactory because we have not explained the discrepancies at day -3 and day 560. It seems most likely that, in addition to the level of turbulence, which we know to vary, that the velocity of the IISM or its anisotropy must also vary with time. In searching for time variations, we need to obtain more information at each epoch because the three primary harmonic coefficients are only capable of constraining s_p and two other parameters. However we can assume that we know s, Ω and $\cos i$. So we need only constrain two more parameters to obtain an independent fit at each epoch. We will show in the following section that this can be done using the full 2-dim frequency-time acf.

4. THE FREQUENCY-TIME STRUCTURE AND LARGE SCALE PHASE GRADIENTS

The dynamic spectra in figure 1 show striking features which are tilted in the frequency-time plane. Such tilted structures have often been seen in pulsar ISS observations (Hewish et al. 1985; Gupta, Rickett & Lyne 1994) and also in simulations of pulsar scattering (Coles et al. 2010). They are due to dispersive refraction in the interstellar medium, which causes a frequency dependent spatial shift in the ISS pattern that is mapped to a frequency dependent time shift by the pulsar velocity. The effect can be seen very clearly in upper panel of Figure 2 where the observed frequency-time (2-dim) acfs show regular changes in slope which are synchronous with the orbital period. We find that this variation can be modeled well with a constant phase gradient through which

the line of sight moves during the pulsar orbit. The modeled acfs are shown in the right panel and are discussed below.

We computed 2-dim acfs for all the observing epochs at both 820 and 1900 MHz. For the 820 MHz observations we were also able to fit models to the 2-dim acfs in all the blocks in each of the 5 epochs, providing estimates for the velocity, anisotropy, spatial scale, and the phase gradient for those five epochs. The block length was 320 sec for MJD 52997, which was sampled at 5 s intervals; for the 4 remaining epochs the sample interval was ≈ 10 s and the blocks were 63 samples. At 1900 MHz the blocks were 630 s, but the fitting was much less successful due to sporadic narrow band RFI and only the observations on MJD 53560 shown in Figures 1 and 2 provided a useful set of acfs.

The computation of the 2-dim acf from each block of data is such that it is tapered by a triangle in time lag but is essentially unbiassed versus frequency lag, because the recorded bandwidth is much wider than that of the ISS. In addition the acf contains a contribution from white noise as a spike at the origin. As described in §3.2 we fit a theoretical model to the temporal acf, which is well sampled, beginning at the first time lag. Then we extrapolate the model back to zero lag to estimate the variance of the ISS. This is used both to replace the acf at zero lag and to normalize the acfs at all frequency and time lags. Correct normalization is essential in obtaining a good fit to the frequency variation because the frequency axis is rather under sampled and the point at the origin is very important in the fit. We computed the theoretical model of the acf with higher resolution than the observations and filtered it to include the effect of finite resolutions in time and frequency and also multiplied it by the triangular taper in time lag.

4.1. *Model Fitting of the frequency-time acf*

As noted in §3.1, the spatial correlation of intensity $C_I(\boldsymbol{\sigma}) = \exp(-D_\phi(\boldsymbol{\sigma}s))$. However, $C_I(\boldsymbol{\sigma}, \Delta\nu)$ is more complex as described in Appendix A. The 2-dim (frequency-time) acf of a dynamic spectrum is $C_I(\boldsymbol{\sigma} = \boldsymbol{V}_{los}\tau, \Delta\nu)$. If $\boldsymbol{V}_{los}$ is constant this 2-dim acf carries no information on spatial anisotropy, but in a binary orbit $\boldsymbol{V}_{los}$ varies over a considerable angular range and it becomes possible to estimate both the anisotropy and the velocity. However, we must also consider the effects of a transverse gradient in ϕ_p which can have a significant effect on $C_I(\boldsymbol{\sigma}, \Delta\nu)$, as commonly seen in the ISS of some pulsars. Such a gradient causes refraction by an angle:

$$\boldsymbol{\theta}_\mathbf{p} = \boldsymbol{\nabla}\phi_\mathrm{p}/k \propto \nu^{-2}. \tag{16}$$

The refraction displaces the ISS pattern by a transverse vector $\boldsymbol{\sigma}_p$ which, due to dispersion, is $\propto \nu^{-2}$. In Appendices A & A.1 we include this refractive shift, assumed to be constant over the pulsar orbit, in the theoretical model.

The model involved the following 8 parameters: $\boldsymbol{\nabla}\phi_\mathrm{p}$, characterized by $\boldsymbol{\sigma}_p$ relative to the orbital x axis; R, and ψ_{AR}; $\Delta\nu_{iss}$ and the time scaling factor V_o/s_0; and the normalized velocities u_x, u_y, defined in equation (14). The fitting is constrained by the harmonic coefficients k_s and k_0 on the date in question. As s and Ω are known, and R and ψ_{AR} are fitting parameters, we can use k_s and k_0 to determine u_x and u_y. Thus only 6 parameters need be fit. However there is a sign ambiguity in u_y, which we resolved by matching its sign to that of the annual variation model shown in figure 6 on that date.

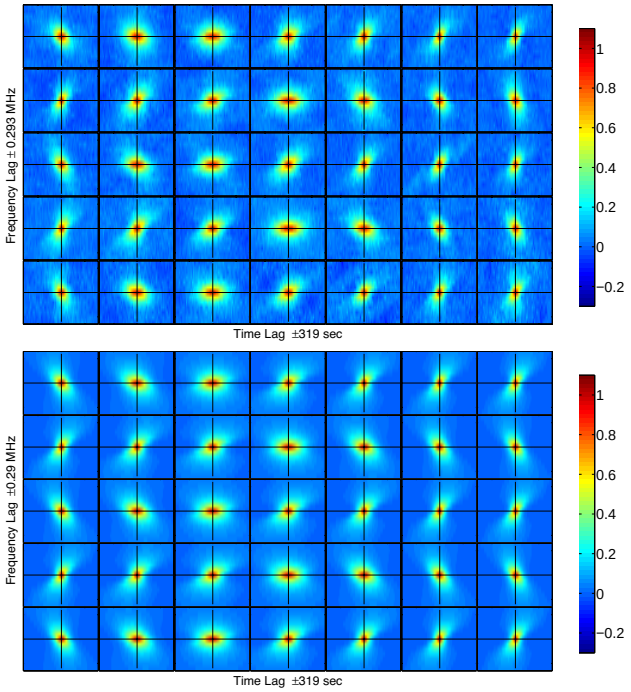

Figure 9. Frequency-time acfs for the 820 MHz dynamic spectra in the lower panel of figure 1. The time lag axis shows ±319 s with triangular tapering over the 320 s block length. The format is the same as Figure 2 but there are 2.5 orbital cycles.

The 820 MHz acf observations on the fifth day are shown in the upper panel of figure 9 in the format of figure 2 with the fitted model in the lower panel. The data on all 5 days at 820 MHz were RFI free and gave good fits to the acf model, as we describe below.

We precomputed a grid of models with anisotropies ($R = 0.05$ 0.22 0.38 0.6 0.8 0.88), and at each R we fitted the remaining 5 parameters with uniform weighting in the frequency-time plane. From the sums-of-squares of the residuals versus R we fitted a parabola to estimate the best-fitting value and its error. In Table 3 we list these with the other fitted parameters and their errors determined at the nearest grid value of R. We also give an estimate of the reduced $\chi^2_{\rm red}$ (row 8), which requires the typical error at each point in the 2-d acf, which was calculated as follows. There are contributions from both system noise ($V_{\rm noise}/\sqrt{N_{\rm noise}}$) and from statistical variations in the ISS ($V_{\rm iss}/\sqrt{N_{\rm iss}}$) which sum in quadrature. While the noise term is independent in each of the pixels of the acf, the ISS term is correlated over the characteristic scales in frequency and time. In the 820 MHz data the ratio of the variance in the ISS to the variance in the noise was in the range $0.1 - 0.2$, such that the ISS and noise made roughly equal contributions to the acf error, which was typically ~ 0.03. The resulting $\chi^2_{\rm red}$ are near unity indicating that the fits are satisfactory.

The 5 anisotropies are somewhat lower than those estimated from the annual variation of the harmonics in Table 2, but are consistent at the 1.5σ level. However there is indication of temporal changes. The $\Delta\nu$ estimates are smaller than or comparable to the 49-kHz channel band-

width of the spectrometer, so they should be considered upper bounds. The s_0 estimates come directly from the model fit. The interstellar velocities are derived from u_x, u_y in the model fit via equation (15), where the listed velocity errors do not include effects of uncertainty in s and Ω. As discussed in §3.3.3 the proper motion velocity of the pulsar system that we used could be too large. However, even the lower estimate of $V_{\mathrm{P}\alpha} = -5.3$, $V_{\mathrm{P}\delta} = 6.2$ km s^{-1} would change the interstellar velocity by their constant vector difference (times $1-s$), which is only about 4 km s^{-1} in magnitude. The last two quantities in Table 3 are calculated from those above. The acf model at 1900 MHz in the lower panel of figure 2 was fitted in a similar fashion, except that the axial ratio was held constant at $A_R = 2$ ($R = 0.6$) and the other 5 parameters were fit. The other observations at 1900 MHz also show ISS slopes and similar behavior. However the data are occasionally corrupted by RFI, which made the fitting unreliable.

Table 3
6 parameters (rows 2-7) were estimated for the 5 observing epochs at 820 MHz from a grid search in R with the fitting errors given assuming R to be correct. Errors in V_{ISx}, V_{ISy} do not include the small systematic errors due to uncertainty in s and in the proper motion of the pulsar binary system; Rows 11 & 12 are derived quantities.

Day	-3	211	311	379	467
R	.43±.02	.40±.04	.17±.05	.49±.02	.19±.03
ψ_{AR} °	48±3	35±3	32±7	53±4	47±5
$\sigma_p(10^9)$m	6.5±.7	11±1	9±1	13 ±2	15±2
ψ_p °	-156±4	16±4	1±6	26±4	-6±1
$\Delta\nu_{iss}$(kHz)	47±2	50±2	44±2	37±2	63±2
$s_0(10^6)$m	3.7±.4	3.5±.3	3.4±.3	3.9±.4	4.2±.4
χ^2_{red}	1.6	1.3	1.3	1.5	1.3
V_{ISx}(km/s)	-1±1	-14±1	-12±1	-12±1	-21±1
V_{ISy}(km/s)	32±1	39±1	41±2	33±2	29±2
$s_{ref}(10^{10}$m)	6.5±.6	5.7±.6	6.4±.6	8.7±.9	5.5±.6
θ_p/θ_d	0.10	0.19	0.14	0.15	0.27

4.2. *Reanalysis of Annual Modulation by the Earth's Motion*

The acf analysis indicates that $\boldsymbol{V_{IS}}$ and the anisotropy is somewhat time variable. Accordingly we modified our annual fitting routine for the harmonics to take variable $\boldsymbol{V_{IS}}$ and anisotropy. The model interpolates linearly between the values found above from the five 820 MHz acf epochs, to obtain the appropriate values for 1900 MHz harmonics. We included the formerly discrepant data from MJD 52997 in the fits.

With variable anisotropy the reduced χ^2 (3.6) was significantly worse than for fits with constant anisotropy. This probably reflects the fact that the mean R from the 820 MHz acfs is somewhat lower than the best fit value of the harmonic fit with constant R. Thus evidence for variable anisotropy on a time scale of a year shown in Table 3 is only marginal.

With variable $\boldsymbol{V_{IS}}$ the fits showed a large improvement. The fits with variable $\boldsymbol{V_{IS}}$ are shown as magenta lines in Figure 6. The revised model now fits the first and last points much better and is equally good in the other points. We conclude that the evidence for variation in $\boldsymbol{V_{IS}}$ on this time scale is strong, and is the cause of the apparent discrepancy on MJD 52997.

We have redone the four harmonic fitting including MJD 52997 using variable $\boldsymbol{V_{IS}}$ to produce "best available" values. In each case we fit s, Ω, R and ψ_{AR}. We used the variable velocity model, or fixed velocities from the previous constant velocity fit. In two cases we held $\cos i = \pm 0.0227$ and in the third case we fit $\cos i$, which yielded $i = 88.1 \pm 0.5°$. The results are given in Table 4. The case for $\cos i > 0$ is compelling as the alternative location doubles the χ^2. It is remarkable how well the location of the scattering medium and the alignment of the pulsar orbital plane are determined. This is because these parameters are not correlated with the inclination.

However, in the fit for i the estimated anisotropy R is significantly larger than the mean from Table 3, and as noted, the fit is worsened by allowing it to vary. This suggests that the uncertainty on the anisotropy is underestimated and weakens the indication of temporal variation in the anisotropy. However the velocity variation must be real and the variations, which are of the order of ±10 km s^{-1}, are probably not super-Alfvénic. However, they suggest that the scattering medium is much less homogeneous than has been assumed.

The fit for the inclination $i = 88.1 \pm 0.5°$ from the variable velocity model agrees at the 1σ level with that assuming a fixed velocity in §3.3.4. It is also consistent with the confidence limits derived from the Shapiro delay at the 1 σ level for $i < 90°$. However the inconsistency in estimating R, ψ_{AR}, discussed above, indicates a weakness in the model, which may contribute a systematic error that is not included in our estimate of i and its standard error.

Table 4
Parameters estimated from fitting to observations of the four normalized harmonic coefficients at 0.8 & 1.9 GHz versus date including MJD 52997 and using a variable IISM velocity model derived from the acf fits.

Parameter	Fit i	$i = 91.3°$	$i = 88.7°$
$\cos i$	0.033 ±0.009	-0.0227	0.0227
s	0.73 ±0.01	0.74 ±.02	0.72 ±0.01
Ω (deg)	62 ± 2	63 ± 3	62 ± 2
R	$0.58 \pm .08$	$0.78 \pm .12$	0.54 ± 0.06
ψ_{AR} (deg)	68 ± 3	75 ± 3	66 ± 3
V_{ISx} (km s^{-1})	variable	variable	variable
V_{ISy} (km s^{-1})	variable	variable	variable
N_{dof}	63	64	64
Reduced χ^2	2.6	5.0	2.7

4.3. *Anisotropy and Phase Gradient Variations*

The phase gradient for each of the five 820 MHz observations is plotted a solid line vector in figure 10. The anisotropy is plotted as dashed line along its major axis on the same figure. One can see that there is some variation in both quantities. Furthermore the mean direction of the phase gradient is nearly parallel or anti-parallel to the mean major axis of the anisotropy. Both quantities would vary randomly even if the IISM were a uniformly turbulent Kolmogorov plasma from refractive effects due to the finite number of scintles in the scattering disc. Hence the variations in both quantities in figure 10 could be due to such statistical variations. However the phase

gradient does show a persistent mean, which is not expected if the turbulence was statistically uniform.

4.4. *Theoretical model for phase gradient variations*

Since the phase gradient $\boldsymbol{\nabla}\phi_{\rm p}$ for the 5 epochs at 820 MHz is well estimated, one can ask if the gradients are typical of what one would expect of a Kolmogorov random process, or if one must invoke a deterministic structure. This is easily done for an isotropic medium and the anisotropy we have measured is not large enough to make a significant difference. The rms phase difference $\phi_{rms}(x)$ over a distance x can be obtained from the structure function of phase directly as $\phi_{rms}(x) = D_\phi(x)^{0.5}$ and the rms gradient would be $\phi_{rms}(x)/x$. Here we have measured $\boldsymbol{\nabla}\phi_{\rm p}$ over s_{ref} so we can compare it with $D_\phi(s_{ref})^{0.5}/s_{ref}$. However it is more intuitive to compare the resulting angular displacement $\boldsymbol{\theta_p}$ with the rms scattering angle $\theta_0 = 1/ks_0$ where $k = 2\pi/\lambda$ is the propagation constant. Substitution yields

$$\mathrm{rms}(\boldsymbol{\theta_p})/\theta_0 = (s_0/s_{ref})^{1/6}. \qquad (17)$$

The scales s_0 and $s_{\rm ref}$ are listed in Table 3 where the bottom row shows that $\theta_p/\theta_0 \sim 0.15 \pm 0.05$. With $s_0/s_{ref} \sim 5 \times 10^{-5}$, the predicted rms value is 0.2 on a refractive timescale $10 - 20$ days. Thus with observations separated by 60-100 days, we are seeing independent samples of a phase gradient which is close to the rms expected from a Kolmogorov spectrum. However it should be noted that comparable phase gradients, lasting for decades, have been observed in other pulsars (Keith et al. 2013). These are due to transverse gradients in the electron column density (dispersion measure), which may be due to a breakdown in the homogeneity of the turbulence or to the presence of a discrete plasma structure somewhere along the line of sight.

4.5. *Theoretical model for anisotropy variations*

The scattering from an isotropic Kolmogorov phase screen will, in any particular realization, appear slightly anisotropic simply because there are a finite number of "scintles" in the scattering disc. This effect has been discussed and quantified by Romani et al. (1986). From their Table 1 one can find an rms value $R \sim 0.7(s_0/s_{ref})^{-1/6}$. If the IISM were isotropic, then from our Table 3 (lines 6 & 7) we would expect an rms $R \sim 0.14$. We actually observe $0.2 < R < 0.5$, which suggests that $R = 0.3 \pm 0.14$ would be a realistic estimate. In this case the variation of ± 0.14 is simply statistical variation in a Kolmogorov medium with a constant anisotropy.

5. THE CROSS CORRELATION BETWEEN THE ISS OF THE TWO PULSARS

In Paper 1 we measured the correlation between the ISS of the two pulsars near the time of A's eclipse, which led to an estimate of the orbital inclination that was even closer to edge-on than found from the timing observations Kramer et al. (2006). However, as Perera et al (2010) have shown, the time windows during each orbit where B is observable have shifted and shrunk due to relativistic precession of B's spin about the orbital angular momentum vector. By 2008 the B pulsar had become undetectable.

We were only able to measure the cross-correlation in the ISS of the pulsars for 6 of the observing epochs. In our interpretation we assume that, where the projected paths of the two pulsars cross, their lines of sight through the IISM to the Earth are identical. In such a situation ISS would cause an identical modulation of intensity versus frequency. Because of the velocities of the center of mass and the Earth relative to the IISM, the paths cross at different times for the two pulsars, but the ISS will be highly correlated if the IISM changes slowly enough.

As in paper 1 we computed the temporal correlation $\rho(t_A, t_B)$ by subtracting the mean and cross-correlating the intensity over frequency from A and B at time offsets t_A and t_B, relative to the center of A's eclipse. The results are shown in Figure 11 for the 6 days that showed significant correlation. $\rho(t_A, t_B)$ is a measure of the correlation between the ISS of the two pulsars $\rho(\mathbf{s} = \mathbf{r_A} - \mathbf{r_B})$ where $\mathbf{r_A} = \mathbf{V_A}t_A$ and $\mathbf{r_B} = \mathbf{V_B}t_B + (0, \mathrm{y_B}(0))$, with the velocities projected transverse to the path through the IISM. Here A's position at its eclipse defines the origin of the x, y coordinates. $(0, \mathrm{y_B}(0))$ is the projected offset of B, where $\mathrm{y_B}(0) = -d_{AB}\cos i$ with d_{AB} their separation at the eclipse. The time offsets (t_A and t_B) are short enough that $\mathbf{V_A}$ & $\mathbf{V_B}$ are effectively constant. The observations show greatest correlation when A is before the eclipse and when B is after the eclipse.

We have overplotted two 50% correlation contours derived from the model developed in previous sections. The two models correspond to orbital inclinations of 89.0° and 91.0° and are plotted as overlapping white and black lines, respectively. Since the observed correlations are normalized by the square root of the product of the total variances in the A and B spectra, the model correlations must be reduced by factors that depend on the signal to noise ratios. The marginal plots of these factors show that the A pulsar flux is steady except when it is eclipsed. However B only turns on for positive t_B, and so correlation is only observed when B is near or after the eclipse. Thus although we were able to detect the correlation on 6 days, there is only one day on which the peak correlation can be measured with any confidence in Figure 11. Only in the first (upper left) panel does B have any significant flux before the eclipse and it is consistent with the white theoretical contour. In the other panels there is no flux in B inside most of the predicted 50% white contour. However where there is measurable B flux the correlation level for the white ellipse is consistent with the prediction. Conversely the black ellipses, ($i = 91°$), are shifted well into the t_B region, yet the correlation is much lower than predicted by the model. In the other observing epochs we observed observed no flux from B for $t_B < 0$ and no AB correlation. Had the inclination been $> 90°$ we should have seen AB correlation.

We have not been able to make a satisfactory estimate for the bias to the correlation due to B's absence before the eclipse and so we cannot define a formal error on the inclination from this investigation. It is clear however that the AB correlations favour the higher end of the range $i = 88.1 \pm 0.5°$ found in §3.3.4. As the inclination is decreased from 89° the white contour in Figure 11 moves to the upper left further from the measured positive correlation. Thus we conclude that the measured temporal correlation $\rho(t_A, t_B)$ is consistent with the model developed earlier and supports the conclusion

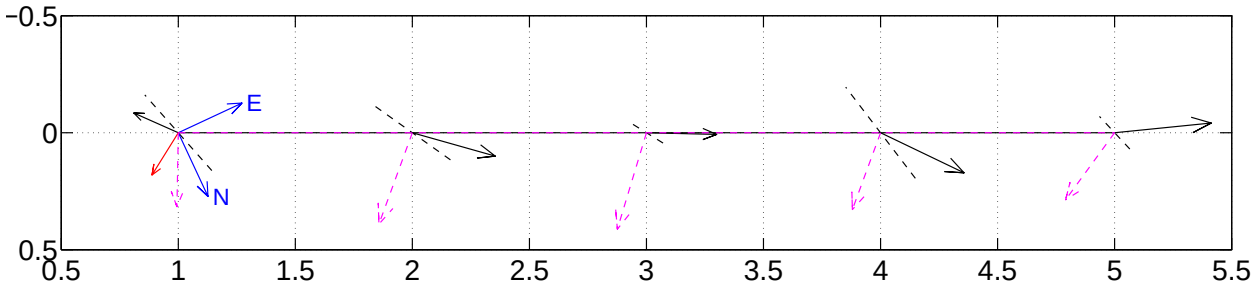

Figure 10. Vector representations of the IISM anisotropy, phase gradient and velocity in the plane of the sky for the 5 epochs observed at 820 MHz. The orbital x-axis (toward the line of nodes) is horizontally to the right and the y-axis is vertically down. Note that with the orbit inclination near 90° its angular momentum vector points upwards in the figure. Celestial North and East are marked by blue arrows on day 1. The major axis of scattering is shown as a black dashed line of length R at angle ψ_{AR} to the x-axis. The black solid arrow is the refractive displacement vector σ_p, ψ_p, (parallel to the transverse phase gradient) as defined in the Appendix (and arbitrarily scaled). The magenta dashed arrows show the interstellar velocity vector. The system proper motion velocity is shown by the red arrow on day 1. The scaling of all velocity vectors is in 100 km s^{-1} units. The Earth's motion round the Sun makes a cycloidal trajectory through the IISM, which complicates a spatial mapping of the 5 epochs.

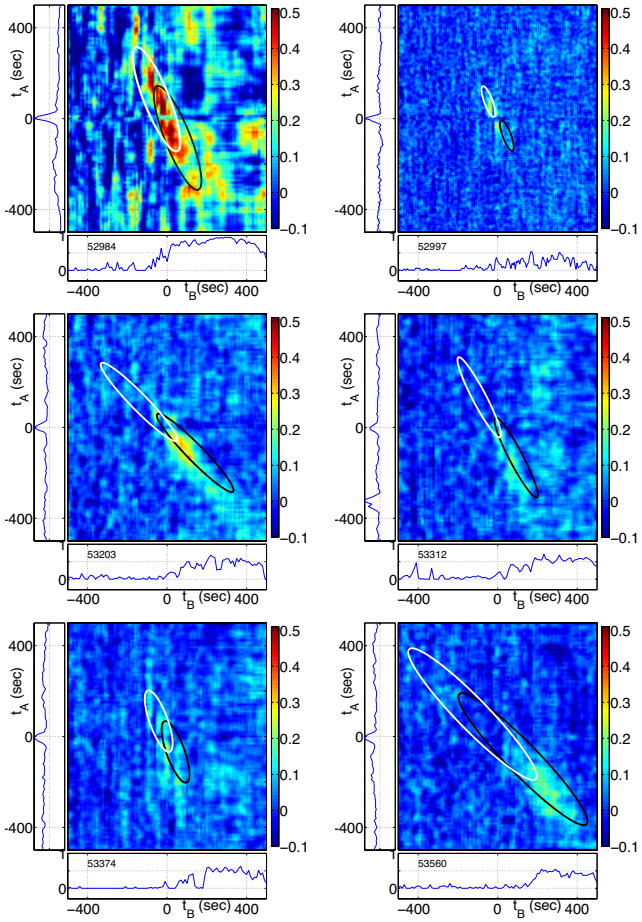

Figure 11. Correlations $\rho(t_A, t_B)$ between the ISS of pulsars A and B on MJDs 52984, 52997, 53203, 53312, 53374, and 53560 at frequencies of 1420, 820, 1950, 1950, 1950, and 1950 MHz working left to right and top to bottom. The plotted coordinates are observing times (t_A, t_B) relative to the time of A's eclipse. The 50% contour of the theoretical models described in the text are shown as white and black ellipses for $i = 89.0°$ and $i = 91.0°$, respectively. The models will be reduced by the factors, shown in the marginal plots, due to the changing signal-to-noise ratios for A and B. The scale in the marginal plots is 0 to 1.0.

that the inclination is $\sim 1°$ less than 90°. However, it does not have the power to improve the accuracy of that model.

6. CONCLUSIONS

Although we were not able to achieve all the original objectives of this experiment, we have been able to determine the orientation of the orbital plane of the system ($\Omega = 65 \pm 2°$ see Table 4) and the inclination of the orbit ($i = 88.1 \pm 0.5°$). The inclination of the orbit is consistent with earlier measurements of the Shapiro delay, if the smaller of the two possible Shapiro delay solutions (88.7°) is taken.

Knowing the orientation of the system relative to its proper motion will allow immediate progress on other scientific problems. The first of these is the nature of the supernova that created the B pulsar. Several attempts have been made to determine the magnitude of the kick to the nascent B neutron star (e.g., Piran & Shaviv (2005); Willems et al. (2006); Stairs et al. (2006)); these involve tracing the path of the binary system back to possible birthplaces in the Galactic Plane, evolving the orbital eccentricity and semi-major axis to the appropriate age, and determining which set of kick magnitudes and directions is compatible with the known properties of the system. Most of these studies point to a small kick and therefore likely very little tilt of the post-supernova orbital plane relative to the pre-supernova one; this is reinforced by the finding that the spin axis of the A pulsar is close to aligned with the orbital angular momentum (Ferdman et al. 2013). Previous work on the evolution of this system did not use a constraint on Ω, as the anisotropy of the IISM prevented a robust determination of the angle at the time (Stairs et al. 2006) Recent modeling (Wong et al. 2010) has found that kicks in the plane of the pre-supernova orbit are preferred over polar kicks; the rather large angle (60°) found here between the Line of Nodes and the proper motion may be at odds with this result. Revised modeling incorporating the constraint on Ω will be presented elsewhere.

The determination of Ω, plus the resolution of the sign ambiguity in $\cos i$, permits a strengthening of the double-pulsar test of preferred-frame effects in semi-conservative theories of gravity (Wex & Kramer 2007). Such effects would produce periodic changes in the longitude of periastron and the eccentricity of the system, in a manner that depends on the orientation of the system relative to the coordinates of the preferred frame. Therefore, the knowledge of the orientation will allow a more precise

limit to be set on the parameters of this theory.

We model the dominant interstellar scattering plasma as a thin layer located at a distance from the pulsar of $73 \pm 1\%$ of the distance to the Earth. The success of this "thin screen" model emphasizes the highly localized distribution of scattering plasma along the line of sight. We also measured its velocity and scattering parameters. The velocity is about 40 km s^{-1} with respect to the Sun, with variations of about 10 km s^{-1}, that are comparable with expected Alfvén speeds. The level of turbulence varied by a factor of two on a time scale of months, much greater than the statistical variation expected due to refractive effects in a homogeneous Kolmogorov random process. At 5 epochs we measured its anisotropy (axial ratio $1.2 - 1.7$) and phase gradient (due to a transverse gradient in the electron column density). There is some significant variability between epochs in both of these parameters; however the variations are at the level one might expect in different refractive realizations of a homogeneous Kolmogorov random process concentrated in a thin layer.

Our results add to the evidence suggesting that the IISM model of homogeneous isotropic Kolmogorov turbulence is no longer adequate. There is accumulating evidence for: anisotropy and intermittency in the turbulence on sub AU scales (Rickett et al. 2002; Dennett-Thorpe & DeBruyn 2003; Tunstov et al. 2013; Hill et al. 2005; Brisken et al. 2010) and for persistent phase gradients (Keith et al. 2013). Evidently this default model of turbulence in the IISM will need to be modified. Apart from the light this throws on the interstellar plasma, turbulence in the IISM is a problem for accurate pulsar timing which is limited in precision by dispersion and scattering (Keith et al. 2013).

The National Radio Astronomy Observatory is facility of the National Science Foundation operated under cooperative agreement by Associated Universities, Inc. Coles and Rickett acknowledge partial support from the NSF under grant AST 0507713. Rickett thanks the Cavendish Astrophysics Group at Cambridge University for their hospitality. Pulsar research at UBC is supported by an NSERC Discovery Grant.

APPENDIX

SPACE-FREQUENCY CORRELATIONS IN THE LIMIT OF STRONG DIFFRACTIVE SCINTILLATION

The theory for $C_I(\boldsymbol{\sigma}, \Delta\nu)$ was reviewed by Lambert & Rickett (1999) and we follow their treatment here. The correlation of intensity is a fourth order moment of scattered electric field. While in general fourth moments cannot be solved analytically, they simplify in the limit of strong diffractive scintillation to the square of second order moments of electric field versus spatial offset $\boldsymbol{\sigma}$ and frequency difference $\Delta\nu$. Here we assume scattering in a thin layer of plasma, i.e. a "phase screen". As noted $C_I(\boldsymbol{\sigma}, \Delta\nu)$ is given by

$$C_I(\boldsymbol{\sigma}, \Delta\nu) = |\Gamma_D(\boldsymbol{\sigma}, \Delta\nu)|^2 \,, \tag{A1}$$

where $\Gamma_D(\boldsymbol{\sigma}, \Delta\nu)$ is the diffractive part of the electric fields covariance. Here $\boldsymbol{\sigma}$ is defined as a transverse distance measured at the screen. The definition of "diffractive" here involves factoring out a term that corresponds to fluctuations of the pulse arrival time. We assume spherical waves from a pulsar at distance z_p beyond a scattering screen which is at a distance z_o from the observer. The pulsar distance is thus $L = z_o + z_p$. Equation (59) of Lambert & Rickett (1999) gives:

$$\Gamma_D(\boldsymbol{\sigma}, z_e; \nu_m, \Delta\nu) = \frac{\nu_m^2}{2\pi i z_e c \Delta\nu} \int\!\!\int_{-\infty}^{\infty} \exp\left[-0.5 D_\phi(\boldsymbol{\sigma}'; \nu_m)\right] \exp\left[i \frac{\nu_m^2}{2 z_e c \Delta\nu} \left|\boldsymbol{\sigma} - \boldsymbol{\sigma}'\right|^2\right] d^2\boldsymbol{\sigma}' \,, \tag{A2}$$

Here $z_e = z_p z_o / L$ and $D_\phi(\boldsymbol{\sigma}'; \nu_m)$ is the structure function of the plasma phase caused by the screen at frequency ν_m and spatial separation $\boldsymbol{\sigma}'$, as given in equation 2.

We change the spatial coordinate to $\boldsymbol{\sigma}'' = \boldsymbol{\sigma}' - \boldsymbol{\sigma}$ and introduce normalized variables:

$$p = [|\boldsymbol{\sigma}''|/s_0]^2 \;\text{ and }\; v = (\Delta\nu/\nu_m)(r_{\rm Fe}^2/s_0^2) \;\text{ where } r_{\rm Fe} = \sqrt{z_e/k_m} \,. \tag{A3}$$

The second moment can then be written in circular coordinates as

$$\Gamma_D(\boldsymbol{\sigma}, z_e; \nu_m, \Delta\nu) = \frac{1}{i 4\pi v} \int_0^\infty e^{ip/2v} \int_0^{2\pi} exp[-0.5(\alpha + \beta\sqrt{p} + \gamma p)^{5/6}] d\theta''\, dp, \tag{A4}$$

$$\begin{aligned} \text{where} \quad \alpha &= (a\sigma_x^2 + b\sigma_y^2 + c\sigma_x\sigma_y)/s_0^2 \\ \beta &= -(2a\sigma_x \cos\theta'' + 2b\sigma_y \sin\theta'' + c(\sigma_x \sin\theta'' + \sigma_y \cos\theta''))/s_0 \\ \gamma &= a\cos\theta''^2 + b\sin\theta''^2 + c\sin\theta''\cos\theta'' \end{aligned} \tag{A5}$$

The θ'' integral is simple to do numerically, but the Fourier-like integral over p requires care as the normalized frequency offset v approaches zero.

Note that the acf versus frequency offset at a single antenna is included as $\boldsymbol{\sigma} = 0, \alpha = 0, \beta = 0$. So we used equation (A4) to compute the normalized frequency decorrelation width, $v_{0.5}$, versus axial ratio, holding s_0 constant. The result is that the higher the axial ratio the narrower the width $v_{0.5}$; for example, an axial ratio 4:1 reduces $v_{0.5}$ to 0.43 compared to 0.96 for an axial ratio of 1:1. Nevertheless, the shape of the acf is only weakly dependent on the axial ratio. Consequently in reporting the decorrelation bandwidths, we fitted the isotropic model and record the frequency offset for a 50% reduction in the acf, since the bias by unknown axial ratio is less than the fitting error.

Effect of refraction and application to the ISS of pulsar A

A constant phase gradient over the scattering disc will cause a refractive shift of the entire diffraction pattern by an angle $\boldsymbol{\theta_p}$ as given in equation (16). This gives rise to a displacement $\boldsymbol{\sigma}_{\rm p} = z_e\boldsymbol{\theta}_{\rm p} \propto \nu^{-2}$. The frequency derivative $d\boldsymbol{\sigma}_{\rm p}/d\nu = -2\boldsymbol{\sigma}_{\rm p}/\nu$. So for a small refractive shift $\Delta\boldsymbol{\sigma}_{\rm p}$ over a small frequency range $\Delta\nu$ we can write $\Delta\boldsymbol{\sigma}_{\rm p} \sim -2\boldsymbol{\sigma}_{\rm p}(\Delta\nu/\nu)$. The time/frequency correlation $C_I(\tau,\delta\nu)$ can then be written

$$C_I(\tau,\delta\nu) = C_I(\boldsymbol{\sigma} = \boldsymbol{V_{\rm A}}t\,(z_o/L) - 2\boldsymbol{\sigma}_{\rm p}(\Delta\nu/\nu),\Delta\nu). \tag{A6}$$

Models computed in this way are shown in the 28 sub-panels of the lower plot of figure 2. Time lag is plotted horizontally and frequency lag vertically. The slopes come from a constant refractive shift which appears to reverse in sign due the changing pulsar velocity over its 2.45 hr orbit.

INFLUENCE OF ANISOTROPY ON FREQUENCY-TIME ACF

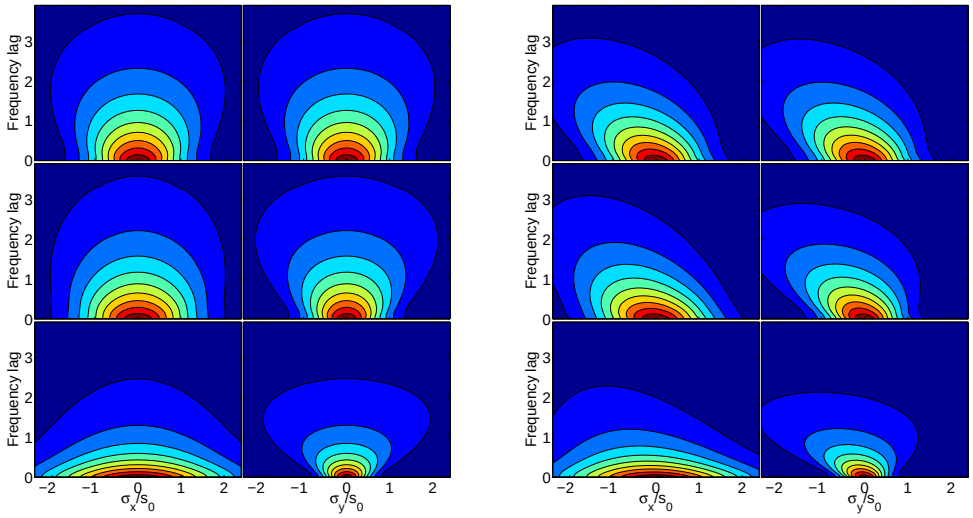

Figure 12. Theoretical acf $C_D(\boldsymbol{\sigma},\Delta\nu)$ for three levels of anisotropy ($R = 0.05, 0.38, 0.88$). Spatial and frequency scales are normalized in units of the corresponding diffractive scales versus σ_x, σ_y. The major axis is along σ_x. Contour levels are at 0.1 through 0.9 in steps of 0.1 and each acf is symmetric about the origin. *Left:* no refraction. *Right:* refractive phase gradient $\theta_{px} = \theta_{py} = \theta_d/2$

The earlier work of Lambert & Rickett (1999) was done for thick and thin screens, but only for isotropic scattering. Here we extend their work to a thin anisotropic screen with a refractive gradient which is constant over the scattering disc. They showed that the shape of contours of constant correlation changed significantly with the level of correlation and this effect was more prominent in thin screens than in thick screens. Here we find that the effect is even more prominent as the anisotropy increases. While the higher level contours near the peak are approximately elliptical, at lower levels they bulge outwards in the spatial coordinate as the frequency offset increases. Of course this is connected with the parabolic arcs which can be seen in the fourier transform of $C_I(\tau,\Delta\nu)$ (Stinebring et al. 2001).

Cuts through $C_I(\boldsymbol{\sigma},\Delta\nu)$ for $\boldsymbol{\sigma} = (\sigma_x, 0)$ (left) and $\boldsymbol{\sigma} = (0,\sigma_y)$ (right) are shown in Figure 12 in the case of no phase gradient (left) and a phase gradient for which $\theta_{px} = \theta_{py} = \theta_d/2$ (right). One can see that the distortion in the shape of the contours persists in the presence of a refractive gradient, that it increases with increasing anisotropy (downwards in the Figure), and that it is quite different in the x and y planes. It is these features that give the frequency-time acfs the potential to estimate both anisotropy and refractive gradient.

Fitting the model acfs

We fitted a model $C_I(\tau,\Delta\nu)$ to the set of observed acfs on a given date of observation. For each data block, centered at orbital phase ϕ, we start with the normalized velocities in equation (14) and write $\boldsymbol{\sigma}(\tau,\Delta\nu)$ as

$$\sigma_x(\tau,\Delta\nu) = (z_o/L)V_o\tau\,(u_x - \sin\phi) - 2\sigma_{px}\nu^{-1}\Delta\nu \;\text{ and }\; \sigma_y(\tau,\Delta\nu) = (z_o/L)V_o\tau\,u_y\sqrt{a/b} - 2\sigma_{py}\nu^{-1}\Delta\nu\ .$$

Here the x-component varies linearly with $\sin\phi$, but the y-component is independent of orbital phase, because with $\cos i$ is so close to zero that V_{Ay} depends only on the center of mass velocity. Thus the combination of the orbital and center of mass motion of the pulsar gives a spatial offset vector (σ_x,σ_y) that swings over a range in angles governed by parameters u_x, u_y. It is this that provides the sensitivity of the ftacf to spatial orientations.

Then we simply substitute the $\boldsymbol{\sigma}$ obtained above in equation (B1). To speed execution we precompute the 3-dim $C_I(\boldsymbol{\sigma},\Delta\nu)$ over a 3-dim grid and find the necessary values of $C_I(\boldsymbol{\sigma}(\tau,\Delta\nu),\Delta\nu)$ by interpolation. The 8 parameters to be determined are: $\Delta\nu_{iss}$ that connects $\Delta\nu$ to v in equation (A3); $u_x; u_y; R; \psi_{AR}; \sigma_p; \psi_p$ & V_o/s_0. u_x, u_y are partially

constrained by the fitting of harmonic coefficients to $T_{\rm ISS}(\phi)$. We proceeded in an iterative fashion also constrained by the results of the annual fitting described in §3.3.

REFERENCES

Armstrong, J.W. & Rickett, B.J., 1981, MNRAS, 194, 623
Armstrong, J. W., Rickett, B. J., & Spangler, S. R. 1995, ApJ, 443, 209 426, 531
Bogdanov, S., Pruszyñska, M., Lewandowski, W. & Wolszczan, A. 2002, ApJ, 581,495
Breton, R. P., Kaspi, Kramer, M. et al. 2008, Science , 321, 104
Breton, R. P., Kaspi, V. M., McLaughlin, et al. 2012, ApJ, 747, 89
Brisken, W. F., Macquart, J.-P., Gao, J. J. et al. 2010, ApJ, 708, 232
Burgay, M., Possenti, A., Manchester, R. N. et al. 2005, ApJ, 624, 113
Coles, Wm.A., McLaughlin, M.A., Rickett, B.J. et al. 2005, ApJ, 623, 392
Coles, W. A., Rickett, B. J., Gao, J. J. et al. 2010, ApJ, 717, 1206
Cordes, J. M. 1986, 311, 183
Cordes, J. M. & Lazio, T. J. W. 2005, astro-ph/0207156
Cordes, J. M. & Rickett, B. J. 1998, ApJ, 507, 846
Deller, A. T., Tingay, S. J., Bailes, M. et al. 2009, ApJ, 701, 1243
Dennett-Thorpe, J. & de Bruyn, A.G. 2003, A&A, 404, 113
Ferdman, R. D., Stairs, I. H., Kramer, M. et al. 2013, ApJ, 767, 85
Grall, R. R., Coles, W. A., Spangler, S. R. et al. 1997, J. Geophys. Res. 102, 263
Gupta, Y., Rickett, B. J. & Lyne, A. G., 1994, MNRAS, 269, 1035
Hemberger, D. A. & Stinebring, D. R., 2008, ApJ, 674, 37
Hewish, A., Wolszczan, A., & Graham, D. A., 1985, MNRAS, 213, 167
Hill, A.,S., Stinebring, D.R., Asplund, C.T. et al. 2005, ApJ, 619, L171
Kaplan, D. L., Escoffier, R. P., Lacasse, R. J. et al. 2005, PASP, 117, 643
Keith, M. J., Coles, W., Shannon, R. M., et al. 2013, MNRAS, 492, 216
Kramer, M., Stairs, I. H., Manchester, R. N. et al. 2006, Science, 314, 97
Lambert, H.C. & Rickett, B.J. 1999, ApJ, 517, 299
Lorimer, D. R. 2001, Arecibo Technical Memo No. 2001–01, see also `http://www.jb.man.ac.uk/~drl/sigproc`
Lovelace, R. V. E., 1970, PhD thesis, Cornell University, Ithaka, NY
Lyne, A. G. 1984, Nature , 310, 300
Lyne, A. G., Burgay, M., Kramer, M. et al. 2004, Science, 303, 1153
Lyutikov, M. & Thompson, C. 2005, ApJ, 634, 1223
Manchester, R. N., Kramer, M., Possenti, A. et al. 2005, ApJ, 621, 49
McLaughlin, M. A., Lyne, A. G., Lorimer, D. R. et al. 2004, ApJ, 616, L131
Ord, S. M., Bailes, M. & van Straten, W. 2002, ApJ, 574, L75
Perera, B. B. P., McLaughlin, M. A., Kramer, M. et al. 2010, ApJ, 721, 1193
Perera, B. B. P., Lomiashvili, D., Gourgouliatos, K. N. McLaughlin, M. A.& Lyutikov, M. et al. 2012, ApJ, 750, 130
Piran, T. & Shaviv, N. J. 2005, Phys.Rev.Lett., 94, 051102
Ransom, S. M., Kaspi, V. M., Ramachandran, R. et al. 2004, ApJ, 609, L71
Rickett, B.J., Kedziora-Chudczer, L. & Jauncey, D.L. 2002, ApJ, 581, 103
Romani R.W., , Narayan, R. & Blandford, R. D. 1986, MNRAS, 220, 19
Stairs, I. H., Thorsett, S. E., Dewey, R. J. et al. 2006, MNRAS, 373L, 50
Stinebring, D. R., McLaughlin, M. A., Cordes, J. M. et al. 2001, ApJ, 549, L97
Tuntsov, A. V., Bignall, H. E. & Walker, M. A. 2013, MNRAS, 429, 2562
Wex, N. & Kramer, M. 2007, MNRAS, 380, 455
Willems, B.; Kaplan, J., Fragos, T. et al. 2006, Phys.Rev.D, 74, 043003.
Wong, T-W., Willems, B., Kalogera, V. 2010, ApJ, 721, 1689
You, X. P., Hobbs, G., Coles, W. A. et al. 2007, MNRAS, 378, 493